ACS APPLIED MATERIALS & INTERFACES

www.acsami.org

Research Article

Machine Learning for Predicting Ultralow Thermal Conductivity and High *ZT* in Complex Thermoelectric Materials

Yuzhou Hao, Yuting Zuo, Jiongzhi Zheng,* Wenjie Hou, Hong Gu, Xiaoying Wang, Xuejie Li, Jun Sun, Xiangdong Ding, and Zhibin Gao*

Cite This: *ACS Appl. Mater. Interfaces* 2024, 16, 47866−47878

Read Online

ACCESS | Metrics & More | Article Recommendations | Supporting Information

ABSTRACT: Efficient and precise calculations of thermal transport properties and figures of merit, alongside a deep comprehension of thermal transport mechanisms, are essential for the practical utilization of advanced thermoelectric materials. In this study, we explore the microscopic processes governing thermal transport in the distinguished crystalline material Tl_9SbTe_6 by integrating a unified thermal transport theory with machine learning-assisted self-consistent phonon calculations. Leveraging machine learning potentials, we expedite the analysis of phonon energy shifts, higher-order scattering mechanisms, and thermal conductivity arising from various contributing factors, such as population and coherence channels. Our finding unveils an exceptionally low thermal conductivity of 0.31 W m^{-1} K^{-1} at room temperature, a result that closely correlates with experimental observations. Notably, we observe that the off-diagonal terms of heat flux operators play a significant role in shaping the overall lattice thermal conductivity of Tl_9SbTe_6, where the ultralow thermal conductivity resembles that of glass due to limited group velocities. Furthermore, we achieve a maximum *ZT* value of 3.17 in the *c*-axis orientation for *p*-type Tl_9SbTe_6 at 600 K and an optimal *ZT* value of 2.26 in the *a*-axis and *b*-axis direction for *n*-type Tl_9SbTe_6 at 500 K. The crystalline Tl_9SbTe_6 not only showcases remarkable thermal insulation but also demonstrates impressive electrical properties owing to the dual-degeneracy phenomenon within its valence band. These results not only elucidate the underlying reasons for the exceptional thermoelectric performance of Tl_9SbTe_6 but also suggest potential avenues for further experimental exploration.

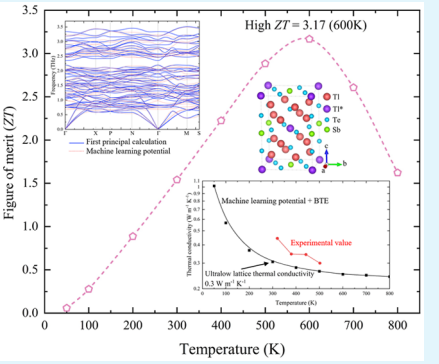

KEYWORDS: *Anharmonic lattice dynamics, Coherent phonons, Lattice thermal conductivity, Moment tensor potential, Band degeneracy, Thermoelectricity*

INTRODUCTION

Thermoelectric materials have the capacity to transform heat into electrical energy without emitting pollutants.[1,2] They lack movable components, generate no noise pollution, and are adjustable in size, rendering them indispensable in a multitude of fields, including waste heat recovery[3] and photovoltaic-photothermal cogeneration.[4] The conversion efficiency of thermoelectric materials can be determined by the figure of merit $ZT = S^2\sigma/(\kappa_e + \kappa_L)$, where S, σ, κ_e, and κ_L are the Seebeck coefficient, electrical conductivity, electronic thermal conductivity and lattice thermal conductivity, respectively. In order to achieve optimal thermoelectric performance, a promising strategy involves enhancing electrical transport while simultaneously suppressing thermal transport.[5] Nevertheless, it is challenging to achieve a high electrical conductivity (σ) and low electronic thermal conductivity (κ_e) simultaneously. Consequently, ultralow lattice thermal conductivity (κ_L) becomes a crucial factor contributing to high thermoelectric efficiency.

Recent studies have identified several materials with relatively complex structures, including $Cu_{12}Sb_4S_{13}$,[6] $AgPbBiSe_3$,[7] $Cs_2BiAgBr_6$,[8] KCu_5Se_3,[9] and Cu_7PS_6.[10] These materials exhibit potential for thermoelectric applications due to their ability to achieve ultralow thermal conductivity (κ_L). Therefore, research on complex thermoelectric materials is not only of fundamental interest but also of crucial importance for the advancement of thermoelectric technology.

The Tl-Te system contains numerous complex materials with an ultralow κ_L. For instance, the κ of $Ag_8Tl_2Te_5$, Ag_9TlTe_5, Tl_9CuTe_5, Tl_2GeTe_3, $TlInTe_2$, etc., are all lower than 0.5 W m^{-1} K^{-1} at room temperature.[11,12] Moreover, the κ of the promising thermoelectric materials Tl_9BiTe_6 and Tl_9SbTe_6 was reported to be 0.5 W m^{-1} K^{-1} and 0.7 W m^{-1} K^{-1}, respectively, at room temperature.[11] Although experiments have shown that Tl_9BiTe_6 exhibits a lower thermal conductivity, it also exhibits high resistivity, which significantly reduces the power factor and constrains its further enhance-

Received: June 1, 2024
Revised: August 25, 2024
Accepted: August 26, 2024
Published: September 2, 2024

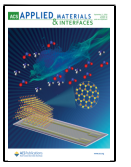

ment as an additional component. Even with minimal Tl_9BiTe_6 incorporation, it can markedly diminish the thermoelectric performance of the material.[13]

Compound Tl_9SbTe_6 represents the material most closely related to Tl_9BiTe_6 within the Tl_5Te_3 family. Its thermal conductivity is comparable to that of Tl_9BiTe_6, yet its electrical conductivity is markedly superior, as evidenced by the experimental results.[11] Although there have been experimental studies on thermoelectric properties[11,14,15] and analysis of electronic structure,[16] there is still a lack of in-depth research on its low κ and high thermoelectric efficiency due to its complex structure. Further comprehensive research will help us better understand and design excellent thermoelectric materials based on a complex Tl-Te system.

Despite the significant advancements in measuring ultralow κ in experiments, theoretical prediction and explanation of ultralow κ in complex compounds remain challenging. Recent studies have explored anharmonic effects as potential sources of discrepancies of κ between the experiment and theory observed in highly anharmonic crystals.[6,17−22] These studies have revealed that lattice anharmonicity significantly influences the phonon line width and lattice thermal conductivity.[23] While the conventional Peierls−Boltzmann framework is adequate for describing phonon transport in systems with well-defined phonon modes, it encounters challenges in highly anharmonic systems.[23,24] Therefore, it becomes imperative to consider the temperature-dependent frequencies evaluated by the self-consistent phonon (SCPH) approach in elucidating thermal transport in complex compounds.[25,26]

Moreover, a discrepancy exists between the experimentally measured and theoretically predicted κ by the conventional Peierls-Boltzmann transport equation.[27] Consequently, it becomes necessary to consider the influence of wavelike interbranch tunneling of coherence, originating from off-diagonal terms of the heat flux operator,[27] to comprehensively explain this phenomenon. Overall, to accurately predict thermal transport properties in complex thermoelectric materials, it is necessary to explicitly evaluate the phonon energy shifts and scattering rates using the higher-order force constants, i.e., fourth-order force constants, and coherent phonons.

Despite the significant achievements in DFT-based thermal conductivity calculations,[28] the computational expense of calculating thermal conductivity considering higher-order phonon scatterings is so high that it is sometimes prohibitive.[29,30] The use of machine Learning Potential (MLP) can significantly reduce the cost of calculating force constants while maintaining considerable computational accuracy.[31] Machine learning potential (MLP) is a method that employs machine learning algorithms to describe the atomic potential energy surface and predict the energy and force based on the atomic environment. Unlike machine learning models (ML-Models),[32] MLP can be combined with BTE methods to provide detailed phonon information, thereby enabling a more comprehensive understanding of the mechanism of thermal transport in the large system. Furthermore, it is capable of calculating complex systems under a multitude of conditions, including those involving impurities and defects[33,34] affecting lattice thermal conductivity and the figure of merit (ZT), as well as disorder, anharmonicity, and other complex systems that are challenging to calculate using DFT methods.

Shapeev et al. developed a machine learning potential function, the moment tensor potential (MTP),[35,36] which achieves a good balance between computational accuracy and computational complexity. MTP can obtain high-precision second- and third-order force constants. According to the previous research, MTP can also obtain reliable fourth-order force constants, which can accurately calculate the κ_L containing four-phonon scattering.[37] Consequently, we modified and developed the corresponding interface using the MTP to obtain fourth-order force constants in an efficient manner.

In this study, we conducted a comprehensive investigation of the thermal transport and thermoelectric properties of benchmark compound Tl_9SbTe_6. To this end, we integrated machine-learning based anharmonic lattice dynamics with an unified theory of thermal transport and momentum relaxation time approximation. This integration included: (1) Construction of a machine-learning potential with DFT-level accuracy for the complex crystalline Tl_9SbTe_6, (2) anharmonically renormalizing phonons using the SCPH approach, (3) evaluation of thermal transport considering both particle-like and wave-like phonon transport channels, (4) application of distinct scattering mechanisms, including acoustic deformation potential (ADP), ionized impurity (IMP) scattering, and polar optical phonon (POP) scattering, to systematically study the electrical transport properties, and (5) exploration of the trend of the thermoelectric property ZT value with carrier concentration and temperature variation.

COMPUTATIONAL METHODS

Structural Optimization and Data Generation. The Vienna Ab initio Simulation Package (VASP) was used to optimize the crystal structure of Tl_9SbTe_6.[38] All first-principles calculations are performed by using the PAW method with LDA exchange-correlation functional.[39] The structure was optimized until forces fell to 0.00001 eV/Åwith the cutoff energy of 600 eV. The cell and the atoms were all fully relaxed in the structural optimization process with the Monkhorst-Pack k-point grids of 7 × 7 × 7 employed.

The *ab initio* molecular dynamics (AIMD) simulations were also performed by using VASP for energy and atomic forces collecting as training data sets. The isobaric−isothermal (NPT) ensemble with a time step of 1 fs was performed for the 2 × 2 × 2 primitive cell of Tl_9SbTe_6 that contains 128 atoms. The 2 × 2 × 2 grid of k points was used. The data set contains 7000 steps in which there are 1000 steps each at temperatures of 10 K, 70 K, 150 K, 300 K, 500 K, 750 K, and 1000 K. We take one out of every five steps to construct the training data set. And we randomly choose 700 steps in the rest four-fifths of the data set to construct the validation data set.

Electronic Transport Property. Using the relaxation time approximation, the electrical transport distribution function via the linearized Boltzmann transport equation (BTE) is expressed as

$$\sigma^{\alpha\beta}(E) = \sum_i \int \frac{d\mathbf{k}}{8\pi^3} \nu_{i\mathbf{k}}^{\alpha} \nu_{i\mathbf{k}}^{\beta} \tau_{i\mathbf{k}}^{el} \delta(E - E_{i\mathbf{k}}) \tag{1}$$

where $\tau_{i\mathbf{k}}^{el}$ and δ are the electronic relaxation time and Dirac delta function. E, $\mathbf{k}$, and i are the electron energy, wave vector, and electronic band index, respectively. In the process of electron−phonon coupling, electrons and phonons must satisfy the conservation of energy and quasi-momentum. Here, the ith electron at the initial state $i\mathbf{k}$ collides with phonons of wave vector $\mathbf{q}$ and phonon frequency $\omega_{\mathbf{q}}$, and it transitions to the final state $j\mathbf{k}+\mathbf{q}$. This scattering process can be defined by the Fermi golden rule with elastic electronic scattering rates

$$\tau_{i\mathbf{k}\to j\mathbf{k}+\mathbf{q}}^{-1} = \frac{2\pi}{\hbar} \left\langle j\mathbf{k}+\mathbf{q} | g_{ij} | i\mathbf{k} \right\rangle^2 \delta(E_{i\mathbf{k}} - E_{j\mathbf{k}+\mathbf{q}}) \tag{2}$$

https://doi.org/10.1021/acsami.4c09043
ACS Appl. Mater. Interfaces 2024, 16, 47866−47878

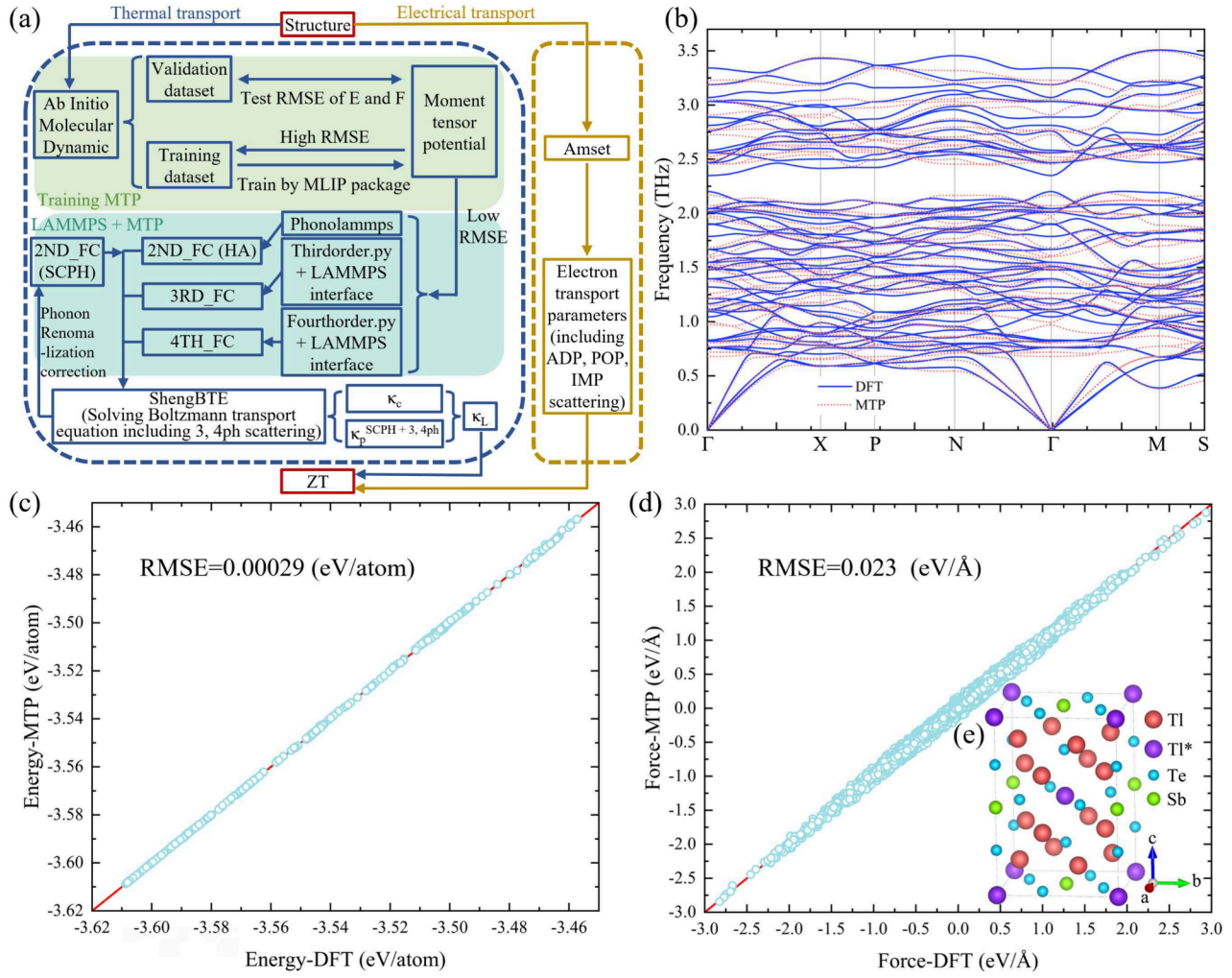

Figure 1. (a) Workflow of the thermoelectric property calculations. (b) Phonon dispersion of Tl_9SbTe_6 calculated by Moment tensor potential (MTP) and DFT. A comparison of (c) the energy per atom (d) and the atomic force between MTP and DFT calculations for Tl_9SbTe_6. (e) The conventional cell structure of Tl_9SbTe_6. The red and purple atoms represent talcium (Tl) atoms in different chemical environments. The atoms represented by the blue color are tellurium (Te) atoms, while the green ones are antimony (Sb) atoms.

or inelastic electronic scattering rates

$$\tau^{-1}_{i\mathbf{k}\to j\mathbf{k}+\mathbf{q}} = \frac{2\pi}{\hbar}\left\langle j\mathbf{k}+\mathbf{q}|g_{ij}|i\mathbf{k}\right\rangle^2 [(n_{\mathbf{q}}+1-f^0_{j\mathbf{k}+\mathbf{q}}) \delta(E_{i\mathbf{k}}-E_{j\mathbf{k}+\mathbf{q}}-\hbar\omega_{\mathbf{q}}) + (n_{\mathbf{q}}+f^0_{j\mathbf{k}+\mathbf{q}})\delta(E_{i\mathbf{k}}-E_{j\mathbf{k}+\mathbf{q}}+\hbar\omega_{\mathbf{q}})] \quad (3)$$

in which f and n are the Fermi−Dirac and Bose−Einstein distributions. g_{ij} is the electron−phonon coupling matrix elements. $\pm\hbar\omega_{\mathbf{q}}$ defines the emission and absorption of a phonon in the scattering process. Here, we consider separated electronic relaxation time for distinct scattering mechanisms,[40] including acoustic deformation potential (ADP), ionized impurity (IMP) scattering, and polar optical phonon (POP) scattering, respectively.

Training Machine Learning Potential. To describe the interatomic interaction, the moment tensor potential (MTP) was trained on the data set generated by the AIMD calculation.[36] The MTP parameters can be fitted by minimizing the function[35]

$$\min \sum_{m=1}^{M}\left[\omega_e(E_m^{\mathrm{AIMD}}-E_m^{\mathrm{MTP}})^2 + \omega_f\sum_{i=1}^{N_f}(f_{m,i}^{\mathrm{AIMD}}-f_{m,i}^{\mathrm{MTP}})^2 + \omega_s(\sigma_m^{\mathrm{AIMD}}-\sigma_m^{\mathrm{MTP}})^2\right] \quad (4)$$

in which E_m^{AIMD} and E_m^{MTP} represent the energy obtained by AIMD and the energy obtained by MTP. Also, f and σ represent atomic force and stress. The factors ω_e, ω_f, ω_s are the weight factors for energy, force, and stress, and they are set to be 1.0, 0.1, and 0.001 respectively. Besides, the cutoff radius was set to 8.0 Å. Since the cutoff values for cubic and quartic interactions used in the phonon thermal conductivity calculations are 5.99 Åand 3.60 Å, smaller than the MLP fitting cutoff radius 8.0 Å, indicating the MLP fitting cutoff radius is sufficiently large for the thermal conductivity calculation. From Figure S3 we can see that the lattice thermal conductivity converges under these cutoff values for cubic and quartic interactions. Furthermore, we used 24.mtp as the initial potential function for training; the radial basis was set to 10, which is greater than the default value of 8, ensuring sufficient accuracy.

Lattice Thermal Conductivity. The lattice thermal conductivity κ_p based on Peierls-Boltzmann transport theory is given by:

$$\kappa_p = \frac{\hbar^2}{k_B T^2 V N_0}\sum_{\lambda} n_\lambda(n_\lambda+1)\omega_\lambda^2 \boldsymbol{v}\lambda \otimes \boldsymbol{v}\lambda\boldsymbol{\tau}_\lambda \quad (5)$$

where $\hbar$ denotes the reduced Planck constant, k_B the Boltzmann constant, T the absolute temperature, V the volume of the primitive unit cell, and N_0 the number of phonon wave vectors sampled in the first Brillouin zone. The variables n_λ, ω_λ, $\boldsymbol{v}_\lambda$, and τ_λ indicate the phonon population, frequency, group velocity, and lifetime for the λ mode which is defined by wave vector q and branch index s.

https://doi.org/10.1021/acsami.4c09043
ACS Appl. Mater. Interfaces 2024, 16, 47866−47878

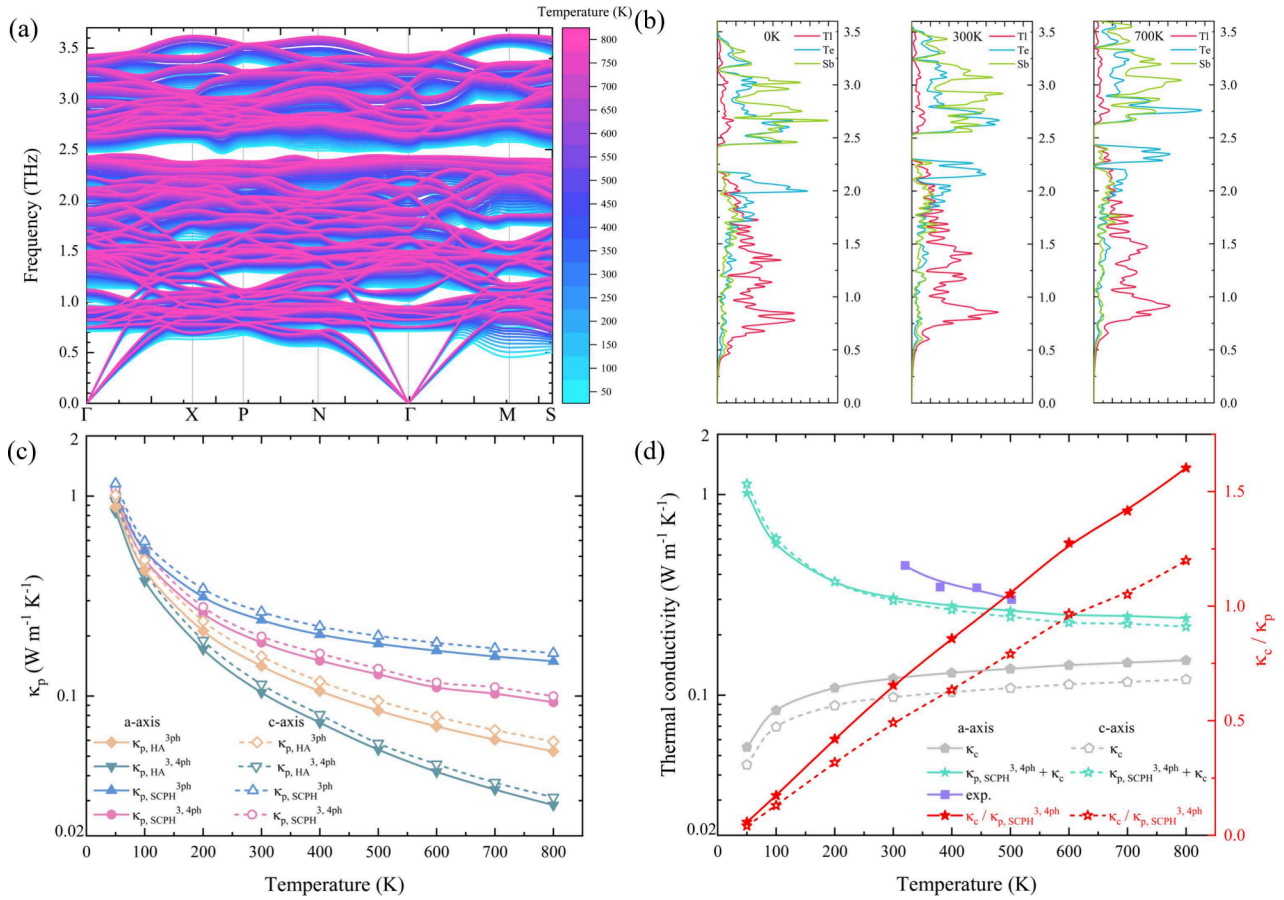

Figure 2. (a) The temperature-dependent phonon spectrum from T = 50 to 800 K for Tl_9SbTe_6. (b) Projected phonon density of states (PDOS) of Tl_9SbTe_6 at 0 K, 300 K, and 700 K. (c) Phonon populations' thermal conductivity (κ_p) as a function of the temperature of Tl_9SbTe_6. (d) Intrinsic lattice thermal conductivity (κ_L) as a function of the temperature of Tl_9SbTe_6. The κ_p in ratio κ_c/κ_p represents $\kappa_{p,SCPH}^{3,4ph}$. The solid lines represent the *a*-axis direction, and the dashed lines represent the *c*-axis direction.

In IFCs calculations, 2 × 2 × 2 primitive cells of Tl_9SbTe_6 were used. For third-order IFCs and fourth-order IFCs calculation, up to the fifth and second nearest neighbors are considered respectively. The q mesh grid was set as 10 × 10 × 10. Also, the SCPH approximation applied in our study serves as an efficient method[23,25] that accurately incorporates the first-order correction of phonon frequencies resulting from quartic anharmonicity. This approach provides a more precise depiction of soft phonon modes and significant anharmonicity. In brief, the SCPH can be expressed as

$$\Omega_\lambda^2 = \omega_\lambda^2 + 2\Omega_\lambda \sum_{\lambda_1} I_{\lambda\lambda_1} \tag{6}$$

where ω_λ represents the initial phonon frequency derived from the harmonic approximation and Ω_λ denotes the temperature-dependent renormalized phonon frequency. The scalar $I_\lambda\lambda_1$ is calculated as follows:

$$I_{\lambda\lambda_1} = \frac{\hbar}{8N_0} \frac{V^{(4)}(\lambda, -\lambda, \lambda_1, -\lambda_1)}{\Omega_\lambda \Omega_{\lambda_1}} [1 + 2n_{\lambda_1}(\Omega_{\lambda_1})] \tag{7}$$

where $V^{(4)}$ represents the fourth-order IFCs in the reciprocal space, and the phonon population n_λ follows the Bose-Einstein distribution. Equations 6 and 7 possess the parameters $I_\lambda\lambda_1$ and Ω_λ, allowing the SCPH equation to be solved iteratively.

To obtain more thorough results for the lattice thermal conductivity, we also considered the off-diagonal terms of the heat-flux operator, which describe the tunneling of coherent phonons. This coherent component κ_c can be expressed as

$$\kappa_c = \frac{\hbar^2}{k_B T^2 V N_0} \sum_{\boldsymbol{q}} \sum_{s \neq s'} \frac{\omega_{\boldsymbol{q}}^s + \omega_{\boldsymbol{q}}^{s'}}{2} \boldsymbol{v}_{\boldsymbol{q}}^{s,s'} \boldsymbol{v}_{\boldsymbol{q}}^{s',s} \times \frac{\omega_{\boldsymbol{q}}^s n_{\boldsymbol{q}}^s (n_{\boldsymbol{q}}^s + 1) + \omega_{\boldsymbol{q}}^{s'} n_{\boldsymbol{q}}^{s'} (n_{\boldsymbol{q}}^{s'} + 1)}{4(\omega_{\boldsymbol{q}}^{s'} - \omega_{\boldsymbol{q}}^s)^2 + (\Gamma_{\boldsymbol{q}}^s + \Gamma_{\boldsymbol{q}}^{s'})^2} \times (\Gamma_{\boldsymbol{q}}^s + \Gamma_{\boldsymbol{q}}^{s'}) \tag{8}$$

where $\hbar$ is the reduced Planck constant, k_B is Boltzmann constant, V is the primitive cell volume, and N_0 is the total number of sampled phonon vectors.

RESULTS AND DISCUSSION

Crystal Structure. The optimized lattice constants of Tl_9SbTe_6, calculated using LDA potentials, are $a = b = 8.63$ Å, and $c = 12.77$ Å. These values are consistent with the experimental values, which are $a = b = 8.830$ Å and $c = 13.013$ Å.[11,16] We also tested different functionals and compared the calculated lattice constants with the experimental measurements, which can be found in Table S1. Additionally, the phonon spectrum calculated using the PBE functional is shown in Figure S5, which contains some imaginary frequencies. As illustrated in Figure 1(b), the phonon spectrum of the LDA functional is devoid of imaginary frequencies, indicating the dynamic stability of Tl_9SbTe_6. The stable structure of Tl_9SbTe_6 is $I4/m$ with space group 87. The primitive cell comprises 16 atoms: one Sb, six Te, and nine Tl. Tl atoms are divided into eight Tl and one Tl*, based on their separate chemical environments and locations, as depicted in Figure 1(e).

https://doi.org/10.1021/acsami.4c09043
ACS Appl. Mater. Interfaces 2024, 16, 47866−47878

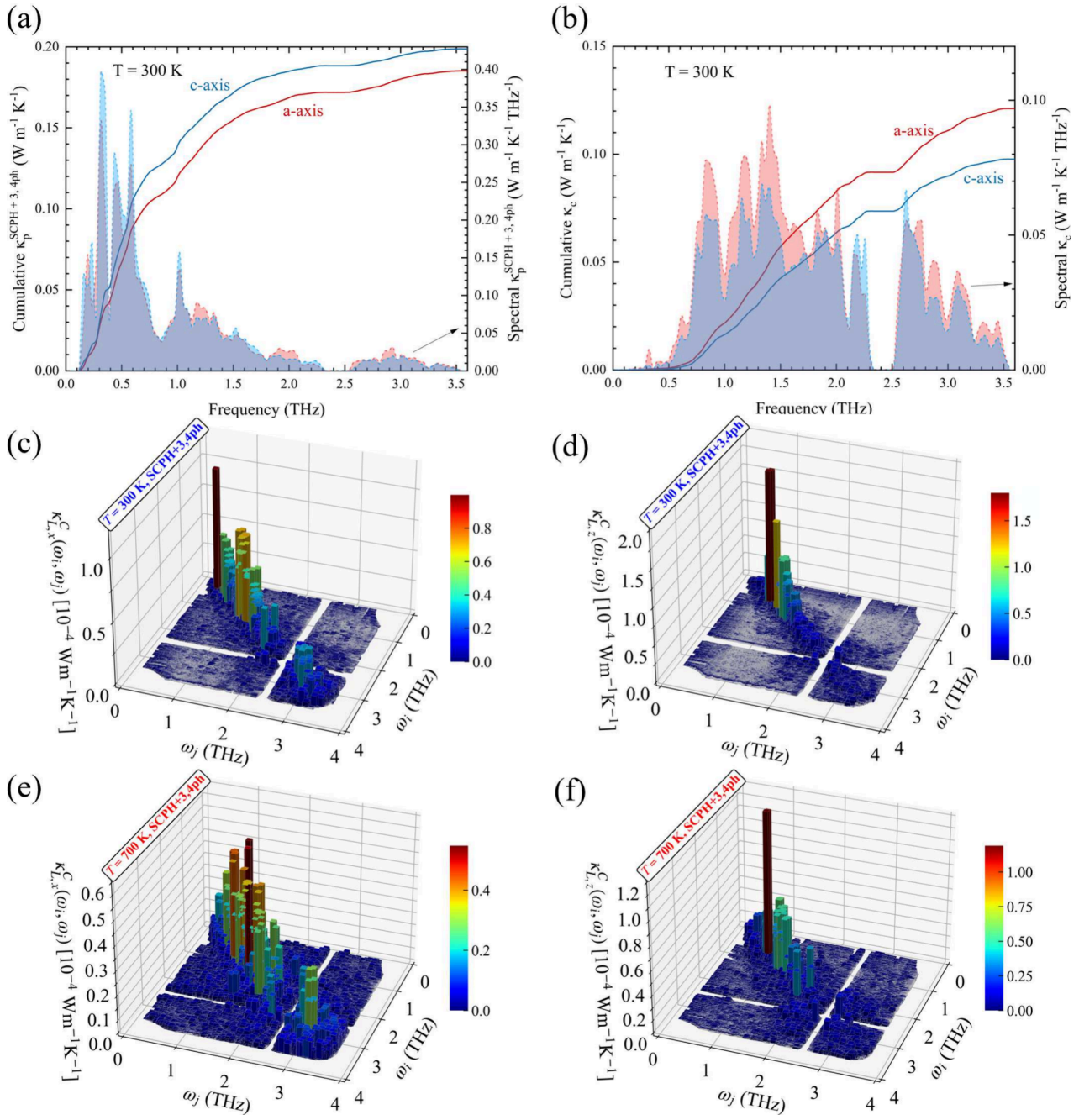

Figure 3. (a) Calculated spectral and cumulative κ_p using the SCPH+3,4ph model at 300 K. (b) Calculated spectral and cumulative coherence thermal conductivities at 300 K. (c) Three-dimensional visualization model $\kappa_c(\omega_i, \omega_j)$ of the contributions to the coherence thermal conductivity in the *a*-axis direction at 300 K. (d) The same as (c) but in the *c*-axis direction. (e) The same as (c) but at 700 K. (f) The same as (d) but at 700 K.

Figure 1(a) depicts the workflow of our work. In this work, we obtain the training data set from *Ab Initio* Molecular Dynamics (AIMD) using the isobaric−isothermal (NPT) ensemble. We then train the MTP and the training principles are detailed in the computational methods section.[35] After obtaining the MTP, we tested it on the validation data set.

The MTP is employed to ascertain the energy and atomic forces of each configuration in the validation data set, with the resulting root-mean-square error (RMSE) being presented in Figure 1(c−d). The RMSE of energy per atom and atomic force is 0.00029 and 0.023 eV/Å, respectively. These values indicate that the trained MTP is sufficiently accurate for calculating thermodynamic properties.[35,37] Furthermore, as shown in Figure 1(b), the phonon spectrum calculated by MTP is in good agreement with the DFT results.

Anharmonic Lattice Dynamics and Thermal Transport Properties. The impact of forth-order anharmonicity on the phonon spectra at finite temperatures is next examined, as depicted in Figure 2(a,b), using the interatomic force constants (IFCs) obtained from MLP. It is evident that overall phonon hardening phenomenon is observed in crystalline Tl_9SbTe_6 as the temperature increases from 50 to 800 K. This observation suggests the presence of strong lattice anharmonicity in Tl_9SbTe_6 and highlights the importance of properly treating lattice anharmonicity in lattice dynamics.[18,20,23,41] In particular, the low-frequency phonons with a frequency below 1.5 Thz are

https://doi.org/10.1021/acsami.4c09043
ACS Appl. Mater. Interfaces 2024, 16, 47866−47878

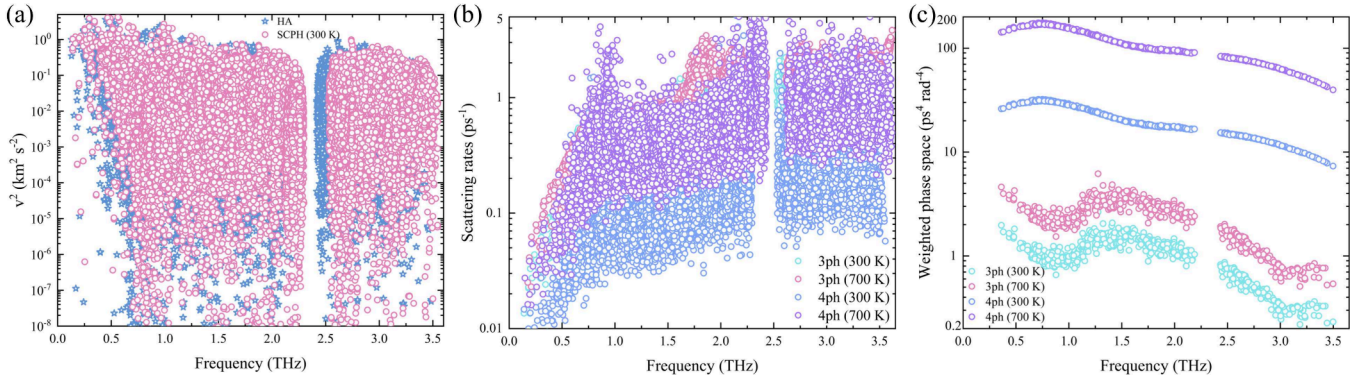

Figure 4. (a) Squared phonon velocities of Tl_9SbTe_6 in the harmonic approximation and the anharmonic renormalization approximation at 300 K. (b) Phonon scattering rates of 3ph and 4ph for Tl_9SbTe_6 at 300 and 700 K. (c) Weighted phonon scattering phase space of 3ph and 4ph for Tl_9SbTe_6 at 300 and 700 K.

predominantly influenced by the Tl atoms, as evidenced by the projected phonon density of states (PDOS) in Figure 2(b). The pronounced phonon hardening observed in the Tl-dominated modes can be attributed to the significant atomic displacements resulting from their loose bonding, as illustrated in Figure S1 in the Supporting Information. We have conducted potential energy as a function of atomic displacement analysis to identify the rattling nature of Tl^+ in Tl_9SbTe_6, confirming the anharmonic rattling behavior and its contribution to the low thermal conductivity. Figure S2 can be written as $y = 1.2593 \times x^4 + 0.0036 \times x^3 + 0.8115 \times x^2$. The result shows that the quartic interaction is very important to the rattling nature of Tl^+. Furthermore, it can be observed that Tl atoms contribute to the low-lying flattened phonon bands in the frequency range of 0.7 to 1.0 THz. This suggests that strong phonon scattering is occurring, which suppresses the primary heat carriers, i.e., acoustic phonon modes.[42−44] In contrast, the optical modes with higher energies exhibit less increase in stiffness, corresponding to the majority of Te and Sb vibrations.

With the zero-K/finite-temperature IFCs at hand, we proceeded to calculate the temperature-dependent κ_p using three different levels of theory, as shown in Figures 2(c,d). It is observed that the lattice thermal conductivity (κ_L) is anisotropic, with the κ_p approximately 10% smaller in the *a*-axis or *b*-axis direction than in the *c*-axis direction. The lowest level of thermal transport theory, namely, the HA+3ph model, yields the following values for $\kappa^{3ph}_{p,HA}$ in the *a*-axis at 50, 300, and 800 K: 0.88, 0.14, and 0.053 W m^{-1} K^{-1}, respectively. As previously stated, anharmonic phonon renormalization is a significant factor in the prediction of the finite-temperature κ_L in complex compounds. With the additional effect of phonon energy shifts, we advance the HA+3ph model to a more accurate SCPH+3ph model, which gives $\kappa^{3ph}_{p,SCPH}$ values of 1.02, 0.24, and 0.15 W m^{-1} K^{-1} at 50, 300, and 800 K, respectively, in the *a*-axis direction. These values are 16%, 71%, and 183% larger than $\kappa^{3ph}_{p,HA}$, indicating significant anharmonic phonon renormalization in Tl_9SbTe_6, with a substantial increase as the temperature rises. This trend is also confirmed by Figure 2(a), which shows significant phonon frequency shifts with an increasing temperature.

In addition, the quartic anharmonicity not only induces significant shifts in phonon frequencies but also results in pronounced 4ph scatterings. Consequently, additional 4ph scatterings were included to obtain $\kappa^{3,4ph}_{p,SCPH}$ values of 0.96, 0.19, and 0.093 W m^{-1} K^{-1} at 50, 300, and 800 K, respectively, in the *a*-axis direction (see Figure 2(c)). These values represent decreases of 6%, 21%, and 38% compared with $\kappa^{3ph}_{p,SCPH}$, indicating the importance of the 4ph scattering processes.[18,44,45] This implies that phonon renormalization and 4ph scattering induced by quartic anharmonicity exert an inverse influence on thermal transport.

Nevertheless, $\kappa^{3,4ph}_{p,SCPH}$ remains considerably lower than the experimentally measured κ_L, as illustrated in Figure 2(d), indicating that coherence contributions are not negligible. By further considering the off-diagonal terms of heat flux operators, the total κ_L significantly enhanced by incorporating both $\kappa^{3,4ph}_{p,SCPH}$ and κ_c.[27]

As illustrated in Figure 2(d), the ratio κ_c/κ_p is greater than 0.5 at 300 K and exhibits a pronounced increase with the temperature. Specifically, in the *a*-axis direction, he ratio of κ_c/κ_p reaches 1.60 at 800 K, which is 2.44 times larger than the 0.65 observed at 300 K. This observation suggests that κ_c is the dominant contribution to κ_L in crystalline Tl_9SbTe_6 at temperatures above 600 K. The dominant role of coherence contribution in thermal transport was also observed in other complex compounds such as $Cs_2AgBiBr_6$,[22] $Cu_{12}Sb_4S_{13}$,[6] $CsPbBr_3$,[46] and even simple cubic CsCl.[45] Although the heat transport phenomena in Tl_9SbTe_6 exhibit similarities to those in glasses, the strong phonon anharmonicity is the key factor contributing to the coherent thermal conductivity. In contrast, in glasses, the off-diagonal contributions arise from structural disorder.

After incorporating κ_c, the total κ_L is approximately 0.27 W m^{-1} K^{-1} and 0.26 W m^{-1} K^{-1} at 400 and 500 K, respectively. This is consistent with experimental measurements, where κ_L is approximately 0.34 and 0.30 W m^{-1} K^{-1} at 400 and 500 K, respectively.[11] In the previous experiment, κ_L is the difference between total thermal conductivity (κ) and electronic thermal conductivity (κ_e), where κ_e is estimated via the Wiedemann−Franz relationship $\kappa_e = L\,\sigma\,T$. The Lorenz number L was calculated by utilizing the single parabolic band and elastic carrier scattering assumption.[11] This implies that the little difference between our κ_L and the experimentally predicted ones is negligible. Additionally, we observed that the dependence of κ on temperature approximately follows $T^{-1/3}$, which indicates the glass-like behavior of crystalline Tl_9SbTe_6.

To gain a deeper insight into the thermal transport in complex crystalline Tl_9SbTe_6, we calculate the spectral and

https://doi.org/10.1021/acsami.4c09043
ACS Appl. Mater. Interfaces 2024, 16, 47866−47878

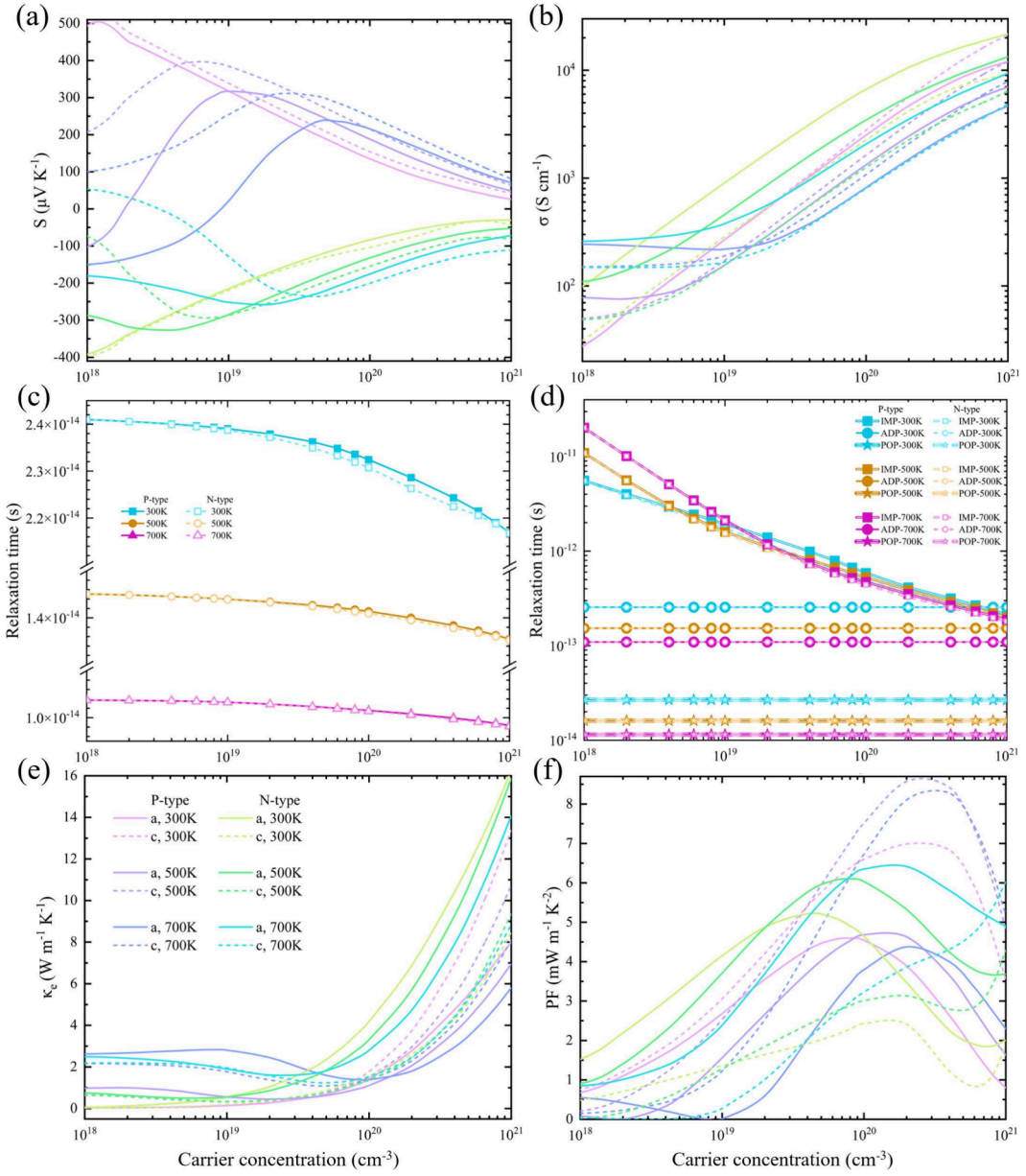

Figure 5. Temperature-dependent (a) Seebeck coefficient S, (b) electrical conductivity σ, (e) electronic thermal conductivity κ_e, and (f) the power factor ($PF = S^2\sigma$) of the Tl_9SbTe_6 were calculated as a function of carrier concentration (holes and electrons) along different axes at 300, 500, and 700 K, respectively. (c) and (d) represent the total and separated electronic relaxation time for distinct scattering mechanisms, including acoustic deformation potential (ADP), ionized impurity (IMP) scattering, and polar optical phonon (POP) scattering, respectively.

cumulative κ_L for both populations' and coherences' contributions, as illustrated in Figure 3(a) and (b). Figure 3(a) shows that the majority of κ_p in Tl_9SbTe_6 is carried by phonons with a frequency below 2 THz at 300 K. Phonons with frequencies below 0.8 THz at 300 K contribute 57% and 62% of κ_p in the *a*-axis and *c*-axis directions, respectively. In contrast, as depicted in Figure 3(b), the majority of κ_c from the wave-like tunneling channel is carried by phonons with a frequency less than 2.4 THz at 300 K. However, phonons with frequencies less than 0.8 THz contribute only 7% of κ_c, due to the good particle-like nature of these low-frequency phonons.[46] Overall, the data presented in Figure 3(a) and (b) indicate that low-frequency phonons predominantly contribute to κ_p, while high-frequency phonons primarily contribute to κ_c.[18,22] This observation can be attributed to the fact that phonon scattering rates increase with increasing temperature in Tl_9SbTe_6, as illustrated in Figure 4(b).

Furthermore, we observe a dip in κ_p and a peak in κ_c around 0.85 THz. This can be attributed to the low-lying flattened modes, which are dominated by Tl atoms with strong phonon−phonon scattering. Due to the strong anharmonicity of these modes, they significantly contribute to the coherence conductivity at this frequency range. Figure 3(c−f) illustrate the contributions to κ_c in Tl_9SbTe_6, calculated using the SCPH +3,4ph model at 300 and 700 K, respectively, and resolved in terms of pair phonon energies. From Figure 3(c−f), it is evident that quasi-degenerate phonons dominate κ_c, with optical phonons (frequencies larger than 0.8 THz) contributing the most. Additionally, it can be observed that the contribution of the couplings between acoustic and optical phonons to κ_c in Tl_9SbTe_6 increases as the temperature rises

https://doi.org/10.1021/acsami.4c09043
ACS Appl. Mater. Interfaces 2024, 16, 47866−47878

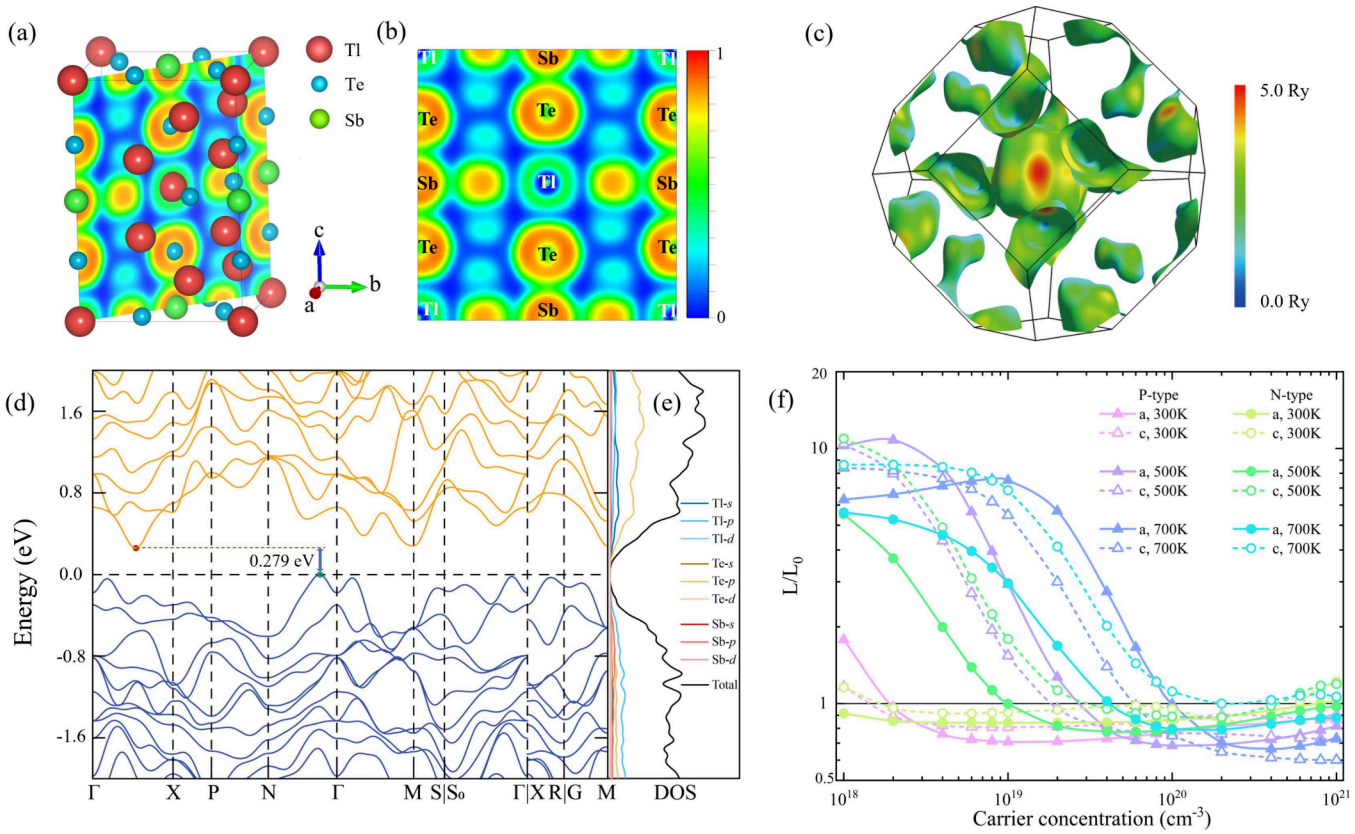

Figure 6. Electron Localization Function (ELF) of Tl_9SbTe_6 in (a) 3D and (b) 2D plots. ELF = 1 corresponds to complete localization, and ELF = 0 corresponds to complete delocalization of electrons. (c) Calculated Fermi surfaces for the valence band structure minimum of Tl_9SbTe_6 in the first Brillouin zone around the Fermi level. (d) Electronic band structure and (e) electronic density of states (DOS) of Tl_9SbTe_6. (f) Normalized Lorenz number as a function of carrier concentration at temperatures of 300 K, 500 and 700 K, respectively. The Lorenz number, denoted by L_0, is a constant that is closely approximately by the Sommerfeld value, $L_0 = 2.44 \times 10^{-8}$ W Ω K^{-1}.

from 300 to 700 K in both the *a* and *c* directions. This phenomenon can be attributed to the observed increase in phonon scattering rates with temperature.

To gain further insight into the microscopic mechanism of the ultralow κ_L in Tl_9SbTe_6, we conducted a detailed study of several parameters closely related to κ_L, including phonon velocities, weighted phonon scattering phase space, and phonon scattering rates. These findings are presented in Figure 4(a–c). Since κ_L is proportional to the square of the phonon group velocity (v^2), we calculate frequency-dependent v^2 where v is the group velocity at 300 K, as shown in Figure 4(a). It can be seen that v^2 of Tl_9SbTe_6 is extremely low, with a maximum value of 5 km^2 s^{-2}. In all directions, the maximum value of v^2 is lower than that of PbTe, which is approximately 14 km^2 s^{-2},[47] with κ_L of 2 W m^{-1} K^{-1} at 300 K. Furthermore, for the ultralow κ_L $Bi_4O_4SeCl_2$, with a thermal conductivity of 0.1 W m^{-1} K^{-1} at 300 K, exhibits the highest velocity of 8 km^1 s^{-1},[30] which is higher than the maximum velocity of Tl_9SbTe_6. Consequently, the ultralow κ in Tl_9SbTe_6 is primarily attributed to the low phonon group velocities.

Furthermore, we observe pronounced scattering rates in crystalline Tl_9SbTe_6, as illustrated in Figure 4(b). In particular, Figure 4(b) clearly shows a strong peak in phonon scattering rates around 0.8 THz, originating from the low-lying flattening modes dominated by Tl atoms [see Figure 2(a)]. In general, the low-lying flattening modes contribute to strong phonon–phonon scattering rates, particularly four-phonon scattering rates, thereby suppressing thermal transport.[42−45] Therefore, the strong phonon scattering rates arising from the loose bonding of Tl atoms are another factor contributing to the ultralow κ value in Tl_9SbTe_6.

To obtain a more comprehensive understanding of phonon scattering rates, we also calculated the phonon scattering phase space, as depicted in Figure 4(c). As illustrated in Figure 4(c), the weighted phase space for both three-phonon (3ph) and four-phonon (4ph) scattering processes increases as the temperature rises from 300 to 700 K. It is evident that the phase space of 4ph processes is larger than that of 3ph processes, resulting in a significant source of 4ph scattering rates in Tl_9SbTe_6. As anticipated, the peak region around 0.75 THz of the 4ph phase space in Tl_9SbTe_6 is in alignment with the partial density of states (PDOS) of Tl atoms, as illustrated in Figure 2(b). As previously discussed, the low-lying flattening modes typically result in elevated 4ph scattering rates by enhancing the 4ph scattering channels. Consequently, this will further suppress thermal transport in Tl_9SbTe_6.

Electronic Transport Properties. The calculated electronic transport coefficients including the Seebeck coefficient *S*, electrical conductivity σ, electronic thermal conductivity κ_e, and the power factor (PF = $S^2\sigma$) of Tl_9SbTe_6 based on the Onsager coefficients are presented shown in Figure 5. For nonpolar crystals, acoustic deformation potential scattering is the main contributor to electric conductivity.[48] Furthermore, we also consider the effects of polar optical phonon scattering[49] and ionized impurity scattering.[40]

https://doi.org/10.1021/acsami.4c09043
ACS Appl. Mater. Interfaces 2024, 16, 47866−47878

Figure 5 presents a depiction of these parameters as functions of carrier concentration at distinct temperatures of 300 K, 500 K, and 700 K, respectively. Notably, Figure 5(a) reveals that both p- and n-type-doped Tl_9SbTe_6 manifest notably elevated Seebeck coefficients S across all investigated temperatures, auguring well for the attainment of enhanced ZT values. For instance, at a temperature of 300 K, the maximal Seebeck coefficients for p- and n-doped Tl_9SbTe_6 materialize at 528 and 393 μV/K, respectively. Our Tl_9SbTe_6 has a Seebeck coefficient that is of a similar order to that of SnSe, which has a favorable 530 μV/K at room temperature.[50]

The Mott formula[51] indicates that the Seebeck coefficient, a crucial parameter in elucidating the interplay between thermal and electrical characteristics in three-dimensional (3D) materials, is expressed as, $S = \frac{2\pi^2 k_B^2 T}{3q\hbar^2}\left(\frac{1}{3\pi^2 n}\right)^{2/3} m^*_{DOS,F}$, where "$n$" and "$m$*" denote the carrier concentration and the effective mass of electron states around the Fermi level. Furthermore, the density of state effective mass is also a function of the band effective mass. The latter is assumed to be a rigid band model, and its dispersion relationship is a standard parabola. They differ by a factor of $N_v^{2/3}$: $m^*_{DOS} = N_v^{2/3} m^*_{band}$, in which N_v is the valley degeneracy.[52] The valley degeneracy of the Tl_9SbTe_6 valence band minimum is two. One is at the M point and the other one is between the Γ and X points, as shown in Figure 6. Therefore, a favorable m_{DOS}* will result in a potential high thermoelectric performance for the Tl_9SbTe_6 material.

Moreover, it can be gleaned from the Mott formula that the Seebeck coefficient for both p- and n-types exhibits a dependence on the temperature and doping concentration. As depicted in Figure 5(a), at lower carrier concentrations, the value of S at 300 K reaches its highest point. However, as the carrier concentration increases beyond a certain threshold, a sequential decline in the Seebeck coefficient from 300 to 700 K is observed, aligning with the anticipated result.

This nonlinear relationship between S and doping concentration stems from the bipolar effect.[53,54] When there are significant number of both electrons and holes contributing to charge transport (bipolar charge transport), the thermoelectric properties are greatly affected. This occurs when electrons are excited across the band gap, producing minority charge carriers (e.g., holes in an n-type material) in addition to majority charge carriers (e.g., the electrons in an n-type material). Bipolar effects are observed in small-band gap materials at high temperatures. Furthermore, it is notable that the Seebeck coefficient of Tl_9SbTe_6 exhibits significant anisotropy, regardless of whether the material is doped with p- or n-type ions.

Figure 5(b) and (e) shows the direct correlation between electrical conductivity σ and electronic thermal conductivity κ_e, as well as carrier concentrations and temperatures of both p- and n-type doping of Tl_9SbTe_6. It can be observed that as temperature increases, conductivity decreases. Conversely, as concentration increases, conductivity increases. Furthermore, Tl_9SbTe_6 exhibits pronounced anisotropy in both electrical conductivity and electronic thermal conductivity, with distinct behaviors observed for p- and n-type doping scenarios. In the context of electron doping, it is evident that the values along the c-axis (dashed lines) are notably lower than those along the a-axis (solid lines). For example, at a temperature of 300 K and a carrier concentration of 10^{20} cm^{-3}, the values of σ and κ_e along the a-axis are 6640.35 S cm^{-1} and 4.18 W m^{-1} K^{-1}, which are approximately three times the values observed along the c-axis with 2254.63 S cm^{-1} and 1.57 W m^{-1} K^{-1}. Conversely, under hole doping conditions, the values along the c-axis are slightly higher than those along the corresponding a-axis.

Figure 5(c) and (d) exhibits the electronic relaxation time (τ_e) for distinct scattering mechanisms, including acoustic deformation potential (ADP), ionized impurity (IMP) scattering, and polar optical phonon (POP) scattering, respectively. It can be seen that the τ_e of IMP is greater than that of ADP, and the τ_e of ADP is greater than that of POP, indicating that POP has the strongest scattering. As the temperature increases, the strength of electron scattering increases, resulting in a corresponding decrease in the τ_e. This is illustrated in Figure 5(c), where the total electronic relaxation time is observed to be on the order of 1×10^{-14} cm^{-3}. As the temperature increases from 300 to 700 K, the electron relaxation time decreases from 2.4×10^{-14} cm^{-3} to 1.0×10^{-14} cm^{-3} for p- and n-type doping Tl_9SbTe_6.

As illustrated in Figure 5(f), the power factor ($S^2\sigma$) was computed based on the Seebeck coefficient and electrical conductivity, under varying temperatures and carrier concentrations. Our findings reveal that Tl_9SbTe_6 exhibits substantial anisotropy in its power factor. Across intermediate temperature and carrier concentration regimes, the power factor for electron-doped Tl_9SbTe_6 along the a-axis consistently surpasses that for hole doping. This indicates that in order to enhance the thermoelectric performance of Tl_9SbTe_6, electron doping is more advantageous than hole doping along the a-axis. In contrast, the effect of hole doping along the c-axis is notably more pronounced and superior in enhancing the power factor. The variation of the power factor with concentration and temperature is not monotonic as a function of electrical and electronic thermal conductivity. The power factor exhibits a characteristic trend whereby it initially rises with increasing carrier concentration and subsequently declines, with a peak concentration range between 10^{20} and 10^{21} cm^{-3} for Tl_9SbTe_6. Below this peak concentration, higher temperatures are associated with lower power factors. It is noteworthy that at a temperature of 500 K and a carrier concentration of 2×10^{20} cm^{-3}, the power factor along the c-axis attains its maximum value, reaching 8.57 mW m^{-1} K^{-2}.

Figure 6(a) and (b) shows the 3D and 2D Electron Localization Functions (ELF) of Tl_9SbTe_6. ELF values of 1 and 0 represent complete localization and delocalization of electrons. The Te and Sb elements exhibit a stronger tendency to attract electrons than the Tl elements, suggesting a greater degree of delocalization for thallium atoms. The delocalized electrons show a stronger electron−phonon coupling.[55,56] This is evident in Figure 2(b), where the thallium element exhibits a very pronounced peak in the low-frequency region (<1.0 Thz) for the phonon density of states.[57,58]

Figure 6(d) and (e) present the electronic band structure and electronic density of state (DOS). We have used the LDA functional to calculate the electronic band structure. Additionally, we have included calculations with DFT-D2 and DFT-D3 corrections. The results are shown in Figure S4. Tl_9SbTe_6 emerges as an indirect bandgap semiconductor, characterized by its conduction band minimum (CBM) positioned between the Γ and X points, and its valence band maximum (VBM) located between the N and Γ points, resulting in a discernible bandgap of 0.279 eV. In the previous work, there are no experimental measurements for the band gap of Tl_9SbTe_6, but

https://doi.org/10.1021/acsami.4c09043
ACS Appl. Mater. Interfaces 2024, 16, 47866−47878

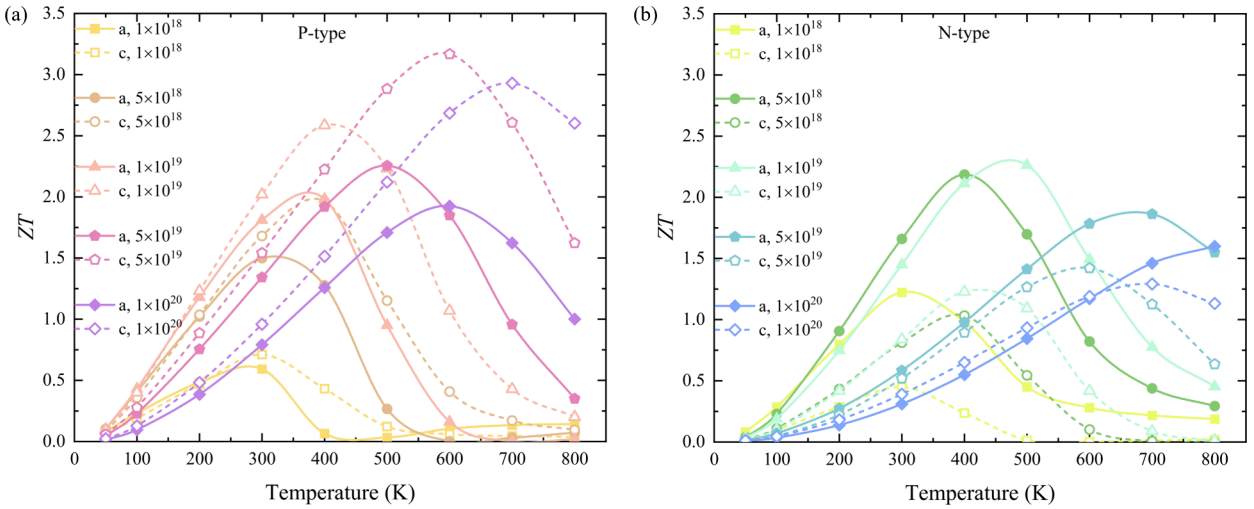

Figure 7. Calculated figure of merit (ZT) of (a) p-type and (b) n-type Tl_9SbTe_6 as a function of temperature along the a- and c- axis at different carrier concentrations, ranging from 1.0×10^{18} cm^{-3} to 1.0×10^{20} cm^{-3}.

a computed value of 0.37 eV[16] is relatively close to our calculated result. The contributions to the bottom of the conduction band and the top of the valence band predominantly arise from the p-orbitals of Te atoms and Tl atoms respectively. Furthermore, the band structure reveals a dual-degeneracy phenomenon within the valence band at the M point. This is also verified by the Fermi surfaces for the valence band structure minimum of Tl_9SbTe_6 in the first Brillouin zone around the Fermi level, as shown in Figure 6(c). Importantly, this observation holds profound significance for enhancing the thermoelectricity ZT of the material, as the insights from band engineering studies.[52,59]

It is well established that electrical transport is not solely dependent on the movement of electrons but also on the transfer of heat. This phenomenon is commonly described by the Wiedemann−Franz (WF) law, which states that the ratio of electrical conductivity to the conductivity of heat (κ_e/σ) is directly proportional to the absolute temperature T. This relationship can be expressed as $\kappa_e/\sigma = LT$, where L is a constant ratio, known as the Lorenz number. The value of L is believed to be close to the Sommerfeld value L_0, which is approximately 2.44×10^{-8} W Ω K^{-1}.[60,61] It is notable that most metals that are considered to be "good" in terms of their conductivity satisfy this WF law. However, the Lorenz number of transition metals such as palladium (Pd), nickel (Ni), cobalt (Co), and platinum (Pt) exhibits larger deviations from the Sommerfeld value L_0.[62,63] Recently, a κ_e that is an order of magnitude lower than expected from the WF law was observed in metallic VO_2 near its insulator−metal transition. This phenomenon was explained in terms of the absence of quasiparticles in a strongly correlated electron fluid in which heat and charge diffuse independently.[60]

The calculated doping-dependent ratio is shown in Figure 6(f). It can be seen that when the doping concentration is high, especially when it exceeds 10^{20} cm^{-3}, L is near equivalent to L_0, exhibiting metallic properties. The lower limit of the doping concentration for the Lorenz number, being close to L_0 increases with temperature. For p-type Tl_9SbTe_6, the lower limit of the doping concentration for the Lorenz number to be close to L_0 at 300 K is around 10^{18} cm^{-3}, while at 700 K it is 6×10^{19} cm^{-3}. This suggests that in order to achieve enhanced thermoelectric performance under high temperature conditions, it may be necessary to adjust the doping concentration within an optimal range.

A higher L value represents a higher ratio of electronic thermal conductivity to electrical conductivity, which is less conducive to improving the thermoelectric properties of the material. At lower concentrations, a substantial deviation of L from the ideal value L_0 is observed, particularly when the concentration is below 5×10^{19} cm^{-3}. Furthermore, the deviation of L from L_0 is more severe with higher temperature than lower temperature. This is consistent with the trend shown in Figure 7, where the lower the doping concentration, the closer the ZT peak value is to the low temperature region. This also makes it difficult to use the Wiedemann−Franz law to predict the κ_L of the material by considering the experimental values of κ and electrical conductivity, as considering L as L_0 will underestimate κ_e, thus overestimate κ_L. Consequently, it is necessary to calculate the Lorenz number L as a function of temperature and doping concentration, which is the prerequisite for accurately estimating thermoelectric performance.

Thermoelectric Performance. The calculated ZT of Tl_9SbTe_6 at different temperatures and doping concentrations is presented in Figure 7. As the doping concentration increases from 1.0×10^{18} cm^{-3} to 1.0×10^{20} cm^{-3}, the peak value of the ZT value will vary from 300 to 700 K and higher, with a greater bias toward higher temperatures. Concurrently, the peak value will initially increase and subsequently decrease, reaching a maximum value at a doping concentration between 5×10^{18} cm^{-3} and 1×10^{19} cm^{-3}. Due to the orientation-dependent properties of phonons and electrons, the ZT value exhibits a significant anisotropy.

In the case of p-type doping, the ZT value in the c-axis direction is significantly higher than that in the a-axis direction, which is the opposite in the case of n-type. At the same temperature, the ZT values of the p- and n-type vary significantly. The highest ZT value of the p-type can reach a peak of 3.17 at 600 K, with a doping concentration of 5×10^{19} cm^{-3}. The highest ZT value of the n-type also reaches a peak of 2.26 at 500 K, with a doping concentration of 1.0×10^{19} cm^{-3}. It can be concluded that the Tl_9SbTe_6 is a highly promising thermoelectric material in the medium temperature zone (300−600 K), particularly for the p-type doping.

https://doi.org/10.1021/acsami.4c09043
ACS Appl. Mater. Interfaces 2024, 16, 47866−47878

CONCLUSION

In conclusion, our study examines the thermal and electrical transport properties of Tl_9SbTe_6 through the integration of machine-learning potential-based self-consistent phonon (SCPH) theory, first-principles calculations, and a unified theory of thermal transport that incorporates both coherence and population conductivities. The Moment Tensor Potential, trained with Machine Learning Interatomic Potential (MLIP), achieves DFT-level accuracy in predicting energy and atomic forces, thereby accurately producing the phonon dispersions for crystalline Tl_9SbTe_6. The force constants derived from the MLIP and SCPH theories indicate a phonon hardening phenomenon across the entire frequency range, which suggests significant lattice anharmonicity in Tl_9SbTe_6. Subsequently, an ultralow κ_L for Tl_9SbTe_6 is predicted, with a value of 0.3 W $m^{-1}K^{-1}$ at room temperature. This value is consistent with the experimentally measured κ_L and exhibits a glass-like temperature dependence.

Our research indicates that four-phonon interaction processes and off-diagonal elements of heat flux operators have a significant impact on thermal transport in Tl_9SbTe_6. Specifically, the four-phonon interaction processes influence phonon energy shifts, which increase the thermal conductivity. However, they also significantly enhance the overall scattering rates, thereby decreasing the thermal conductivity. Furthermore, we observe that in crystalline Tl_9SbTe_6 at temperatures above 600 K, the coherent component κ_c represents the dominant contributor to the lattice κ_L, with a κ_c/κ_p ratio exceeding 1. By analyzing the electronic band structure, we find that Tl_9SbTe_6 also exhibits excellent electrical transport properties, attributed to the dual-degeneracy phenomenon within the valence band.

Our investigation has revealed that Tl_9SbTe_6, with a maximum figure of merit (ZT) of up to 3.17, is a promising candidate for thermoelectric applications. This is due to the ultralow κ_L and favorable electrical transport properties. We have also elucidated the origins of the ultralow κ_L and relatively high electrical conductivity in Tl_9SbTe_6. This involved confirming its optimal charge carrier concentration and operating temperature range. Our study offers insights into potential improvements and application directions for the Tl_5Te_3 family of materials and paves the way to accelerate the accurate prediction of thermoelectric materials.

ASSOCIATED CONTENT

Supporting Information

The Supporting Information is available free of charge at https://pubs.acs.org/doi/10.1021/acsami.4c09043.

Mean square atomic displacements (MSDs) with temperature for Tl_9SbTe_6 (Figure S1), anharmonic frozen-phonon potential with quadratic and polynomial fitting (Figure S2), the lattice thermal conductivity as a function of cutoff distances (Figure S3), the electronic band gap with different computational functionals (Figure S4), phonon dispersion of Tl_9SbTe_6 calculated by DFT using PBE functionals (Figure S5), the calculated lattice constants using different functionals (Table S1), and the crystal structure of the Tl_9SbTe_6 (PDF)

AUTHOR INFORMATION

Corresponding Authors

Jiongzhi Zheng − *Thayer School of Engineering, Dartmouth College, Hanover, New Hampshire 03755, United States; Department of Mechanical and Aerospace Engineering, The Hong Kong University of Science and Technology, Kowloon 999077, Hong Kong;* orcid.org/0000-0001-9841-7477; Email: jiongzhi.zheng@dartmouth.edu

Zhibin Gao − *State Key Laboratory for Mechanical Behavior of Materials, School of Materials Science and Engineering, Xi'an Jiaotong University, Xi'an 710049, China;* orcid.org/0000-0002-6843-381X; Email: zhibin.gao@xjtu.edu.cn

Authors

Yuzhou Hao − *State Key Laboratory for Mechanical Behavior of Materials, School of Materials Science and Engineering, Xi'an Jiaotong University, Xi'an 710049, China*

Yuting Zuo − *State Key Laboratory for Mechanical Behavior of Materials, School of Materials Science and Engineering, Xi'an Jiaotong University, Xi'an 710049, China*

Wenjie Hou − *Institute of Fundamental and Frontier Sciences, University of Electronic Science and Technology of China, Chengdu 610054, China; Taizhou Key Laboratory of Minimally Invasive Interventional Therapy and Artificial Intelligence, Taizhou 317502, China*

Hong Gu − *Suzhou Laboratory, Jiangsu 215123, China*

Xiaoying Wang − *State Key Laboratory for Mechanical Behavior of Materials, School of Materials Science and Engineering, Xi'an Jiaotong University, Xi'an 710049, China*

Xuejie Li − *State Key Laboratory for Mechanical Behavior of Materials, School of Materials Science and Engineering, Xi'an Jiaotong University, Xi'an 710049, China*

Jun Sun − *State Key Laboratory for Mechanical Behavior of Materials, School of Materials Science and Engineering, Xi'an Jiaotong University, Xi'an 710049, China*

Xiangdong Ding − *State Key Laboratory for Mechanical Behavior of Materials, School of Materials Science and Engineering, Xi'an Jiaotong University, Xi'an 710049, China*

Complete contact information is available at: https://pubs.acs.org/10.1021/acsami.4c09043

Author Contributions

Y. Hao, Y. Zuo, and J. Zheng contributed equally to this work.

Notes

The authors declare no competing financial interest.

ACKNOWLEDGMENTS

We acknowledge the support from the National Natural Science Foundation of China (No. 12104356, No. 52250191, No. 12104236), the Opening Project of Shanghai Key Laboratory of Special Artificial Microstructure Materials and Technology (No. Ammt2022B-1), and the Fundamental Research Funds for the Central Universities. J. Zheng acknowledges the support from the National Natural Science Foundation of China (No. 52476070). H. Gu acknowledges the support from Gusu Leading Talent (No. ZXL2021383). This work is sponsored by the Key Research and Development Program of the Ministry of Science and Technology (No. 2023YFB4604100). We also acknowledge the support by HPC Platform, Xi'an Jiaotong University.

REFERENCES

(1) Snyder, G.; Toberer, E. Complex thermoelectric materials. *Nat. Mater.* **2008**, *7*, 105−114.
(2) Zebarjadi, M.; Esfarjani, K.; Dresselhaus, M. S.; Ren, Z. F.; Chen, G. Perspectives on thermoelectrics: from fundamentals to device applications. *Energy Environ. Sci.* **2012**, *5*, 5147−5162.
(3) Baxter, J.; et al. Nanoscale design to enable the revolution in renewable energy. *Energy Environ. Sci.* **2009**, *2*, 559−588.
(4) Dallan, B. S.; Schumann, J.; Lesage, F. J. Performance evaluation of a photoelectric-thermoelectric cogeneration hybrid system. *Sol. Energy* **2015**, *118*, 276−285.
(5) Nolas, G. S.; Sharp, J.; Goldsmid, H. J. *Thermoelectrics: Basic Principles and New Materials Developments*, 1st ed.; Springer: Berlin, 2010; Chapter 6, pp 177−207.
(6) Xia, Y.; Ozoliņš, V.; Wolverton, C. Microscopic Mechanisms of Glasslike Lattice Thermal Transport in Cubic $Cu_{12}Sb_4S_{13}$ Tetrahedrites. *Phys. Rev. Lett.* **2020**, *125*, 085901.
(7) Dutta, M.; Pal, K.; Waghmare, U. V.; Biswas, K. Bonding heterogeneity and lone pair induced anharmonicity resulted in ultralow thermal conductivity and promising thermoelectric properties in n-type $AgPbBiSe_3$. *Chem. Sci.* **2019**, *10*, 4905−4913.
(8) Haque, E.; Hossain, M. A. Origin of ultra-low lattice thermal conductivity in Cs_2BiAgX_6 (X = Cl, Br) and its impact on thermoelectric performance. *J. Alloys Compd.* **2018**, *748*, 63−72.
(9) Li, F.; Liu, X.; Ma, N.; Yang, Y.-C.; Yin, J.-P.; Chen, L.; Wu, L.-M. Overdamped Phonon Diffusion and Nontrivial Electronic Structure Leading to a High Thermoelectric Figure of Merit in KCu_5Se_3. *J. Am. Chem. Soc.* **2023**, *145*, 14981−14993.
(10) Shen, X.; Ouyang, N.; Huang, Y.; Tung, Y.-H.; Yang, C.-C.; Faizan, M.; Perez, N.; He, R.; Sotnikov, A.; Willa, K.; Wang, C.; Chen, Y.; Guilmeau, E. Amorphous-Like Ultralow Thermal Transport in Crystalline Argyrodite Cu_7PS_6. *Adv. Sci* **2024**, *11*, 2400258.
(11) Guo, Q.; Chan, M.; Kuropatwa, B. A.; Kleinke, H. Thermoelectric properties of Sn- and Pb-doped Tl_9BiTe_6 and Tl_9BiTe_6. *J. Appl. Phys.* **2014**, *116*, 183702.
(12) Yamanaka, S.; Kurosaki, K.; Kosuga, A.; Goto, K.; Muta, H. Extremely low thermal conductivity substances as novel thermoelectric materials. *Mater. Res. Soc. Symp. Proc.* **2005**, *886*, 337.
(13) Teubner, J. T. Optimization of high efficiency thermoelectrics based on Tl_5Te_3. Ph.D. thesis, Universität Konstanz, Fachbereich Physik, 2001.
(14) Guo, Q.; Chan, M.; Kuropatwa, B. A.; Kleinke, H. Enhanced Thermoelectric Properties of Variants of Tl_9SbTe_6 and Tl_9BiTe_6. *Chem. Mater.* **2013**, *25*, 4097−4104.
(15) Guo, L. B.; Ye, L.; Wang, Y. X.; Yang, J. M.; Yan, Y. L.; Ren, F. Z. The electronic structure and thermoelectric properties of $BiTl_9Te_6$ and $SbTl_9Te_6$: First-principles calculations. *J. Appl. Phys.* **2015**, *118*, 235703.
(16) Tao, X.; Jund, P.; Viennois, R.; Tedenac, J.-C. Physical Properties of Thallium-Tellurium Based Thermoelectric Compounds Using First-Principles Simulations. *J. Phys. Chem. A* **2011**, *115*, 8761−8766.
(17) Xia, Y.; Pal, K.; He, J.; Ozoliņš, V.; Wolverton, C. Particlelike Phonon Propagation Dominates Ultralow Lattice Thermal Conductivity in Crystalline Tl_3VSe_4. *Phys. Rev. Lett.* **2020**, *124*, 065901.
(18) Wang, X.; Gao, Z.; Zhu, G.; Ren, J.; Hu, L.; Sun, J.; Ding, X.; Xia, Y.; Li, B. Role of high-order anharmonicity and off-diagonal terms in thermal conductivity: A case study of multiphase $CsPbBr_3$. *Phys. Rev. B* **2023**, *107*, 214308.
(19) Tadano, T.; Tsuneyuki, S. Quartic Anharmonicity of Rattlers and Its Effect on Lattice Thermal Conductivity of Clathrates from First Principles. *Phys. Rev. Lett.* **2018**, *120*, 105901.
(20) Zheng, J.; Shi, D.; Yang, Y.; Lin, C.; Huang, H.; Guo, R.; Huang, B. Anharmonicity-induced phonon hardening and phonon transport enhancement in crystalline perovskite $BaZrO_3$. *Phys. Rev. B* **2022**, *105*, 224303.
(21) Yue, J.; Zheng, J.; Li, J.; Guo, S.; Ren, W.; Liu, H.; Liu, Y.; Cui, T. Ultralow Glassy Thermal Conductivity and Controllable, Promising Thermoelectric Properties in Crystalline o-$CsCu_5S_3$. *ACS Appl. Mater. Interfaces* **2024**, *16*, 20597−20609.
(22) Zheng, J.; Lin, C.; Lin, C.; Hautier, G.; Guo, R.; Huang, B. Unravelling ultralow thermal conductivity in perovskite $Cs_2AgBiBr_6$: dominant wave-like phonon tunnelling and strong anharmonicity. *npj Comput. Mater.* **2024**, *10*, 4941−4948.
(23) Tadano, T.; Tsuneyuki, S. Self-consistent phonon calculations of lattice dynamical properties in cubic $SrTiO_3$ with first-principles anharmonic force constants. *Phys. Rev. B* **2015**, *92*, 054301.
(24) Zhao, Y.; Zeng, S.; Li, G.; Lian, C.; Dai, Z.; Meng, S.; Ni, J. Lattice thermal conductivity including phonon frequency shifts and scattering rates induced by quartic anharmonicity in cubic oxide and fluoride perovskites. *Phys. Rev. B* **2021**, *104*, 224304.
(25) Xia, Y.; Hegde, V. I.; Pal, K.; Hua, X.; Gaines, D.; Patel, S.; He, J.; Aykol, M.; Wolverton, C. High-Throughput Study of Lattice Thermal Conductivity in Binary Rocksalt and Zinc Blende Compounds Including Higher-Order Anharmonicity. *Phys. Rev. X* **2020**, *10*, 041029.
(26) Kang, J. S.; Wu, H.; Li, M.; Hu, Y. Intrinsic Low Thermal Conductivity and Phonon Renormalization Due to Strong Anharmonicity of Single-Crystal Tin Selenide. *Nano Lett.* **2019**, *19*, 4941−4948.
(27) Simoncelli, M.; Marzari, N.; Mauri, F. Unified theory of thermal transport in crystals and glasses. *Nat. Phys.* **2019**, *15*, 809−813.
(28) Li, W.; Carrete, J.; A. Katcho, N.; Mingo, N. ShengBTE: A solver of the Boltzmann transport equation for phonons. *Comput. Phys. Commun.* **2014**, *185*, 1747−1758.
(29) Han, Z.; Yang, X.; Li, W.; Feng, T.; Ruan, X. FourPhonon: An extension module to ShengBTE for computing four-phonon scattering rates and thermal conductivity. *Comput. Phys. Commun.* **2022**, *270*, 108179.
(30) Tong, Z.; Pecchia, A.; Yam, C.; Dumitrică, T.; Frauenheim, T. Glass-like Transport Dominates Ultralow Lattice Thermal Conductivity in Modular Crystalline $Bi_4O_4SeCl_2$. *Nano Lett.* **2023**, *23*, 9468−9473.
(31) Mortazavi, B.; Podryabinkin, E. V.; Novikov, I. S.; Rabczuk, T.; Zhuang, X.; Shapeev, A. V. Accelerating first-principles estimation of thermal conductivity by machine-learning interatomic potentials: A MTP/ShengBTE solution. *Comput. Phys. Commun.* **2021**, *258*, 107583.
(32) Wan, X.; Feng, W.; Wang, Y.; Wang, H.; Zhang, X.; Deng, C.; Yang, N. Materials Discovery and Properties Prediction in Thermal Transport via Materials Informatics: A Mini Review. *Nano Lett.* **2019**, *19*, 3387−3395.
(33) Li, G.; Wang, Q.; Cui, Z.; Guo, R. Competition between intrinsic and extrinsic phonon scatterings in cubic BP and BAs with point defects. *Phys. Rev. B* **2023**, *107*, 184118.
(34) Guo, R.; Lee, S. Mie scattering of phonons by point defects in IV-VI semiconductors PbTe and GeTe. *Materials Today Physics* **2020**, *12*, 100177.
(35) Novikov, I. S.; Gubaev, K.; Podryabinkin, E. V.; Shapeev, A. V. The MLIP package: moment tensor potentials with MPI and active learning. *Mach. Learn. Sci. Technol.* **2021**, *2*, 025002.
(36) Shapeev, A. V. Moment Tensor Potentials: A Class of Systematically Improvable Interatomic Potentials. *Multiscale Model. Simul.* **2016**, *14*, 1153−1173.
(37) Ouyang, Y.; Yu, C.; He, J.; Jiang, P.; Ren, W.; Chen, J. Accurate description of high-order phonon anharmonicity and lattice thermal conductivity from molecular dynamics simulations with machine learning potential. *Phys. Rev. B* **2022**, *105*, 115202.
(38) Kresse, G.; Furthmüller, J. Efficient iterative schemes for ab initio total-energy calculations using a plane-wave basis set. *Phys. Rev. B* **1996**, *54*, 11169−11186.
(39) Kohn, W.; Sham, L. SELF-CONSISTENT EQUATIONS INCLUDING EXCHANGE AND CORRELATION EFFECTS. *Phys. Rev.* **1965**, *140*, A1133−A1138.
(40) Ganose, A. M.; Park, J.; Faghaninia, A.; Woods-Robinson, R.; Persson, K. A.; Jain, A. Efficient calculation of carrier scattering rates from first principles. *Nat. Commun.* **2021**, *12*, 2222.

https://doi.org/10.1021/acsami.4c09043
ACS Appl. Mater. Interfaces 2024, 16, 47866−47878

(41) Feng, M.; Wang, X.; Zhu, G.; He, C.; Sun, J.; Ding, X.; Shiomi, J.; Xia, Y.; Li, B.; Gao, Z. The relation between the atomic mass ratio and quartic anharmonicity in alkali metal hydrides. *Mater. Today Phys.* **2024**, *44*, 101423.
(42) Li, W.; Mingo, N. Ultralow lattice thermal conductivity of the fully filled skutterudite $YbFe_4Sb_{12}$ due to the flat avoided-crossing filler modes. *Phys. Rev. B* **2015**, *91*, 144304.
(43) Zheng, J.; Shi, D.; Liu, S.; Yang, Y.; Lin, C.; Chang, Z.; Guo, R.; Huang, B. Effects of high-order anharmonicity on anomalous lattice dynamics and thermal transport in fully filled skutterudite $YbFe_4Sb_{12}$. *Phys. Rev. Mater.* **2022**, *6*, 093801.
(44) Wang, Y.; Gao, Z.; Wang, X.; Sun, J.; Feng, M.; Hao, Y.; Li, X.; Zhao, Y.; Ding, X. Anomalous thermal conductivity in 2D silica nanocages of immobilizing noble gas atom. *Appl. Phys. Lett.* **2024**, *124*, 122205.
(45) Wang, X.; Feng, M.; Xia, Y.; Sun, J.; Ding, X.; Li, B.; Gao, Z. Revisiting lattice thermal conductivity of CsCl: The crucial role of quartic anharmonicity. *Appl. Phys. Lett.* **2024**, *124*, 172201.
(46) He, Y.; Matei, L.; Jung, H. J.; McCall, K. M.; Chen, M.; Stoumpos, C. C.; Liu, Z.; Peters, J. A.; Chung, D. Y.; Wessels, B. W.; Wasielewski, M. R.; Dravid, V. P.; Burger, A.; Kanatzidis, M. G. High spectral resolution of gamma-rays at room temperature by perovskite $CsPbBr_3$ single crystals. *Nat. Commun.* **2018**, *9*, 1609.
(47) Tian, Z.; Garg, J.; Esfarjani, K.; Shiga, T.; Shiomi, J.; Chen, G. Phonon conduction in PbSe, PbTe, and $PbTe_{1-x}Se_x$ from first-principles calculations. *Phys. Rev. B* **2012**, *85*, 184303.
(48) Bardeen, J.; Shockley, W. Deformation Potentials and Mobilities in Non-Polar Crystals. *Phys. Rev.* **1950**, *80*, 72−80.
(49) Fröhlich, H. *Electrons in lattice fields. Adv. Phys.* **1954**, *3*, 325−361.
(50) Zhao, L.-D.; Lo, S.-H.; Zhang, Y.; Sun, H.; Tan, G.; Uher, C.; Wolverton, C.; Dravid, V. P.; Kanatzidis, M. G. Ultralow thermal conductivity and high thermoelectric figure of merit in SnSe crystals. *Nature* **2014**, *508*, 373−377.
(51) Mahan, G. D.; Sofo, J. O. The best thermoelectric. *Proc. Natl. Acad. Sci.* **1996**, *93*, 7436−7439.
(52) Pei, Y.; Shi, X.; LaLonde, A.; Wang, H.; Chen, L.; Snyder, G. J. Convergence of electronic bands for high performance bulk thermoelectrics. *Nature* **2011**, *473*, 66−69.
(53) Zhu, R.; Gao, Z.; Liang, Q.; Hu, J.; Wang, J.-S.; Qiu, C.-W.; Wee, A. T. S. Observation of anisotropic magnetoresistance in layered nonmagnetic semiconducting $PdSe_2$. *ACS Appl. Mater. Interfaces* **2021**, *13*, 37527−37534.
(54) Gong, J.; Hong, A.; Shuai, J.; Li, L.; Yan, Z.; Ren, Z.; Liu, J.-M. Investigation of the bipolar effect in the thermoelectric material $CaMg_2Bi_2$ using a first-principles study. *Phys. Chem. Chem. Phys.* **2016**, *18*, 16566−16574.
(55) Gao, Z.; Zhu, T.; Sun, K.; Wang, J.-S. Highly anisotropic thermoelectric properties of two-dimensional As_2Te_3. *ACS Appl. Electron. Mater.* **2021**, *3*, 1610−1620.
(56) Qin, F.; Wang, X.; Hu, L.; Jia, N.; Gao, Z.; Aydemir, U.; Chen, J.; Ding, X.; Sun, J. Switch of thermal expansions triggered by itinerant electrons in isostructural metal trifluorides. *Inorg. Chem.* **2022**, *61*, 21004−21010.
(57) Gao, Z.; Wang, J.-S. Thermoelectric penta-silicene with a high room-temperature figure of merit. *ACS Appl. Mater. Interfaces* **2020**, *12*, 14298−14307.
(58) Gao, Z.; Liu, G.; Ren, J. High thermoelectric performance in two-dimensional tellurium: An ab initio study. *ACS Appl. Mater. Interfaces* **2018**, *10*, 40702−40709.
(59) Liu, W.; Tan, X.; Yin, K.; Liu, H.; Tang, X.; Shi, J.; Zhang, Q.; Uher, C. Convergence of Conduction Bands as a Means of Enhancing Thermoelectric Performance of n-Type $Mg_2Si_{1-x}Sn_x$ Solid Solutions. *Phys. Rev. Lett.* **2012**, *108*, 166601.
(60) Lee, S.; Hippalgaonkar, K.; Yang, F.; Hong, J.; Ko, C.; Suh, J.; Liu, K.; Wang, K.; Urban, J. J.; Zhang, X.; Dames, C.; Hartnoll, S. A.; Delaire, O.; Wu, J. Anomalously low electronic thermal conductivity in metallic vanadium dioxide. *Science* **2017**, *355*, 371−374.
(61) Wang, W. O.; Ding, J. K.; Schattner, Y.; Huang, E. W.; Moritz, B.; Devereaux, T. P. The Wiedemann-Franz law in doped Mott insulators without quasiparticles. *Science* **2023**, *382*, 1070−1073.
(62) Tong, Z.; Li, S.; Ruan, X.; Bao, H. Comprehensive first-principles analysis of phonon thermal conductivity and electron-phonon coupling in different metals. *Phys. Rev. B* **2019**, *100*, 144306.
(63) Zhang, X.; Li, S.; Wang, A.; Bao, H. Pressure-dependent thermal conductivity in Al, W, and Pt: Role of electrons and phonons. *Phys. Rev. B* **2022**, *106*, 094313.

https://doi.org/10.1021/acsami.4c09043
ACS Appl. Mater. Interfaces 2024, 16, 47866−47878